

Revisiting the Radial Metallicity Gradient-Age Relation in the Milky Way’s Thin and Thick Disks

AO CHEN,^{1,2,3} JUNTAI SHEN,^{1,2,3} CHUN WANG,⁴ AND YANG HUANG^{5,6}

- ¹*Department of Astronomy, School of Physics and Astronomy, Shanghai Jiao Tong University, 800 Dongchuan Road, Shanghai 200240, People’s Republic of China*
²*State Key Laboratory of Dark Matter Physics, School of Physics and Astronomy, Shanghai Jiao Tong University, Shanghai 200240, People’s Republic of China*
³*Key Laboratory for Particle Astrophysics and Cosmology (MOE)/Shanghai Key Laboratory for Particle Physics and Cosmology, Shanghai 200240, People’s Republic of China*
⁴*Tianjin Astrophysics Center, Tianjin Normal University, Tianjin 300387, People’s Republic of China*
⁵*School of Astronomy and Space Science, University of Chinese Academy of Sciences, Beijing, People’s Republic of China*
⁶*New Cornerstone Science Laboratory, National Astronomical Observatories, Chinese Academy of Sciences, Beijing, People’s Republic of China*

ABSTRACT

Galactic disks typically exhibit a negative radial metallicity gradient, indicating faster enrichment in the inner regions. Recent studies report that this gradient becomes flatter with increasing stellar age in the Milky Way’s (MW) thin disk, while the thick disk exhibits a mildly positive gradient across all ages. In this work, we revisit the metallicity gradient–age relation (MGAR) in both the thin and thick disks of the MW. We use spectroscopic data from LAMOST DR8 and stellar ages calibrated with asteroseismology. Our results show a steadily flattening MGAR in the thin disk and confirm a positive gradient $\sim 0.013 \text{ dex kpc}^{-1}$ in the thick disk. The flattening in the thin disk may be caused by large-scale radial migration induced by transient spiral arms, or by a time-dependent steepening of the interstellar medium (ISM) metallicity gradient as suggested by recent FIRE2 simulations. The positive gradient in the thick disk may reflect early enrichment of the outer regions by strong feedback or starburst-driven outflows in a turbulent, gas-rich proto-disk. These findings suggest distinct chemodynamical evolution paths for the MW’s thin and thick disks and provide valuable constraints for future models of Galactic chemical evolution.

Keywords: Milky Way dynamics (1051) — Milky Way disk (1050) — Milky Way evolution (1052)

1. INTRODUCTION

A cornerstone of galaxy evolution is the negative radial metallicity gradient, which describes the decrease in stellar metallicity with increasing galactocentric radius. [Matteucci & Francois \(1989\)](#) reproduced this trend using “inside-out” formation models, in which the inner disk forms stars more rapidly and enriches earlier than the outer regions. This scenario naturally results in a negative metallicity gradient for stars formed from the interstellar medium (ISM, [Matteucci 2021](#)). Following

this framework, [Minchev et al. \(2018\)](#) found that the ISM gradient flattens over time as the outer disk becomes progressively enriched and approaches the central metallicity.

In this context, we refer to the *stellar birth gradient* as the radial metallicity gradient imprinted on stars at their formation, which inherits from the corresponding ISM gradient. Reconstructing the time sequence of these birth gradients would require direct knowledge of the metallicity distribution of newly formed stars at each epoch, which is not directly observable. Instead, what we can measure today is the metallicity gradient of mono-age stellar populations. By using stellar age as a proxy for look-back time, these present-day gradients give rise to the *metallicity gradient–age relation* (MGAR). It is also important to note that the present-day radial distribution of a mono-age stellar population

Corresponding author:

jtshen@sjtu.edu.cn

wchun@tjnu.edu.cn

huangyang@ucas.ac.cn

does not necessarily preserve the distribution of their birth radii, as stars can migrate significantly over their lifetimes. Consequently, the observed MGAR is shaped by both the time evolution of the stellar birth gradient and the subsequent dynamical history of the Milky Way (MW).

The pioneering study on the MGAR in our MW by Mayor (1976) measured a mean radial metallicity gradient of $-0.05 \pm 0.01 \text{ dex kpc}^{-1}$, which steepens to $-0.10 \pm 0.02 \text{ dex kpc}^{-1}$ for younger stars. Using effective temperature (T_{eff}) of main-sequence stars as a proxy for age, Yu et al. (2012) found that the gradient steepens with increasing T_{eff} (typically associated with decreasing age), but shows no trend for stars with $T_{\text{eff}} < 6,000 \text{ K}$ —those with main-sequence lifetimes $\gtrsim 10 \text{ Gyr}$. These early findings hinted at a flattening gradient for increasingly older stars in the MW’s thin disk.

Large-scale spectroscopic surveys have greatly facilitated precise age estimates, enabling direct MGAR measurements (e.g., Vickers et al. 2021; Wang et al. 2023b; Ratcliffe et al. 2023). Vickers et al. (2021, hereafter V21) used LAMOST DR5 and reported a flattening gradient in the thin disk, starting at $-0.075 \text{ dex kpc}^{-1}$ for the youngest stars and flattening with a rate of $0.003 \text{ dex kpc}^{-1} \text{ Gyr}^{-1}$. They also found a slightly positive gradient of $\sim 0.02 \text{ dex kpc}^{-1}$ for all ages in the thick disk, consistent with constantly positive gradients of old, cool main-sequence stars ($T_{\text{eff}} < 6,000 \text{ K}$) in Yu et al. (2012), which are likely from the thick disk.

Radial migration has been proposed as a major process that alters stellar positions and flattens metallicity gradients (Sellwood & Binney 2002). This mechanism, sometimes dubbed “churning”, causes significant radial mixing; non-axisymmetric perturbations such as transient spiral arms can induce large-scale stellar migration by exchanging stars across the corotation radius. In contrast, “blurring” refers to orbital heating that increases the amplitude of stellar epicycles without changing their guiding centers. Churning flattens the MGAR as older stars have had more time to migrate, resulting in a flatter radial metallicity distribution.

Recent simulations support the impact of radial migration. Lu et al. (2024) and Ratcliffe et al. (2023) analyzed the correlation between $[\text{Fe}/\text{H}]$ spreads and stellar birth gradients in mono-age simulated populations, and recovered a time-dependent flattening of birth gradients. Anders et al. (2023) further compared observed MGAR from APOGEE DR17 with modeled ISM gradients evolution from Ratcliffe et al. (2023) to demonstrate the role of migration.

However, the migration interpretation has been challenged by recent FIRE2 simulations (Graf et al. 2024,

2025). They found that present-day MGARs closely follow the stellar birth gradient with minimal influence from churning in these simulations. As gas-phase metal gets mixed before star formation, the role of churning is significantly weakened.

Moreover, Graf et al. (2024) argued that vertical evolution—where turbulent gas settles over time, known as the “upside-down” scenario—may play a more dominant role than inside-out radial growth in shaping Galactic chemo-dynamical history. This suggests the need to consider vertical processes and possible differences in the evolutionary pathways of the thin and thick disks, as also done by V21.

To constrain the MGAR in the MW’s thin and thick disks, we follow an approach similar to V21. We isolate “pure” thin and thick disk populations using both geometric and chemical criteria, and compute MGAR separately for each population. Stellar kinematics and abundances are taken from LAMOST DR8 (Wang et al. 2022a), and stellar ages are calibrated from asteroseismic data provided by the *Kepler* mission (Wang et al. 2023a), offering an alternative to traditional isochrone fitting.

This paper is organized as follows. Section 2 describes the data selection, disk classification, orbital calculation, and gradient fitting method. Section 3 presents the MGAR measurements in both the thin and thick disks. Section 4 discusses the implications of our results and compares MGAR in the thin disk to the literature. Section 5 summarizes our conclusions.

2. DATA AND METHOD

The Large Area Multi-Object Spectroscopic Telescope (LAMOST), located at Xinglong Station of the National Astronomical Observatory of China, is a 4-meter Schmidt telescope with a 5° field of view. It is one of the most extensive stellar spectroscopic surveys and has released 13 data sets to date. In this work, we use LAMOST Data Release 8 (DR8; Wang et al. 2022a) combined with stellar ages from Wang et al. (2023a), which trained a neural network using asteroseismic data from the LAMOST-*Kepler* survey.

Our cross-matched sample contains 986,405 unique stars: 688,369 red giant branch (RGB) stars and 298,036 red clump (RC) stars, each with 6D phase-space coordinates, $[\text{Fe}/\text{H}]$, $[\alpha/\text{Fe}]$, and age measurements. This study treats RGB and RC stars as a single population. We have also tested the MGAR trends separately for RGB and RC stars and found that the qualitative trends remain unchanged.

2.1. Quality Cuts and Orbital Parameters

The main source of uncertainty in the MGAR arises from stellar age measurements. To minimize the contamination from binary evolution or mass transfer, we remove stars with masses $< 0.7 M_{\odot}$ (Wang et al. 2023a). Since the age estimates have a typical uncertainty floor of $\sim 20\%$ (Wang et al. 2023a), we exclude stars with age uncertainties exceeding 30%. We have verified that applying a stricter 25% cutoff yields similar results.

Additional quality criteria include signal-to-noise ratio $\text{SNR} > 20$, vertical distance $|Z| < 10 \text{ kpc}$, and Galactocentric radius $5 \text{ kpc} < R < 20 \text{ kpc}$. We require `flag_feh_apogee=0` and `flag_afe_apogee=0` to exclude stars with unreliable $[\text{Fe}/\text{H}]$ or $[\alpha/\text{Fe}]$ estimates outside the training grid. To avoid halo contamination, we retain only stars with $[\text{Fe}/\text{H}] \geq -1.0 \text{ dex}$ and $v_{\phi} \geq 0$.

We further exclude stars with relative uncertainty $> 40\%$ in any of the spatial or velocity parameters $X \in \{r, v_r, v_{\phi}, z, v_z\}$, i.e., we require

$$\left| \frac{\Delta X}{X} \right| < 40\% \text{ for all } X.$$

These quality cuts result in a clean sample of 246,671 stars.

To mitigate the impact of orbital blurring, we follow V21 and compute gradients using the Galactocentric radius of the guiding center R_g . R_g and the maximum vertical excursion Z_{max} are calculated using the Galactic potential model `MWPotential2014`, implemented in the `galpy` package (Bovy 2015). We adopt the solar position $R_0 = 8.27 \text{ kpc}$ and circular velocity $v_0 = 236 \text{ km s}^{-1}$ (Schönrich & Aumer 2017). Figure 1 shows the distributions and selection criteria (next Section) used for defining thin/thick disk subsamples.

2.2. Thin/Thick Disk Subsamples

The MW’s disk can be separated into two components, either geometrically (via vertical excursion) or chemically (via $[\alpha/\text{Fe}]$ – $[\text{Fe}/\text{H}]$ bimodality). Geometrically, the MW’s stellar density profile can be decomposed into two exponential components (e.g., Gilmore & Reid 1983). In the $[\alpha/\text{Fe}]$ – $[\text{Fe}/\text{H}]$ plane, there are two distinct sequences (e.g., Hayden et al. 2015); such a chemical bimodality reflects differences in nucleosynthetic timescales (Nomoto et al. 2013). The α -rich sequence is associated with rapid early star formation dominated by Type II supernovae, which produce more α elements (e.g., ^{16}O , ^{20}Ne , ^{24}Mg , ^{28}Si) relative to ^{56}Fe . In contrast, Type Ia supernovae, with their longer delay times, enrich more Fe relative to α and contribute more to the α -poor (solar-like) sequence (Binney & Tremaine 2008).

As argued by V21, using chemical and geometric cuts together more effectively isolates the flattening MGAR

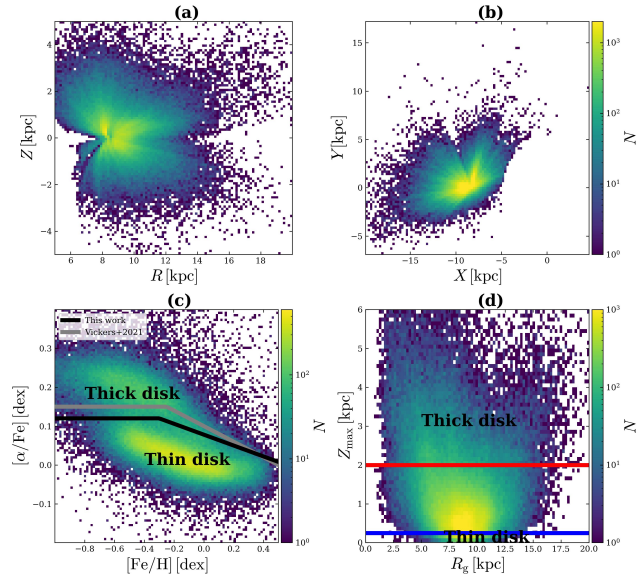


Figure 1. Spatial and chemical distributions of the selected clean LAMOST DR8 sample. (a): Galactic meridional distribution. (b): Face-on view of the sample. (c): Number density in the $[\alpha/\text{Fe}]$ – $[\text{Fe}/\text{H}]$ plane. The black line shows our chemical separation between the thin and thick disks ($[\alpha/\text{Fe}] = 0.12$ for $[\text{Fe}/\text{H}] < -0.3$, otherwise $[\alpha/\text{Fe}] = 0.12 - 0.14([\text{Fe}/\text{H}] + 0.3)$). The gray line indicates the V21 separation, which is not optimal for our sample. (d): Number density in the Z_{max} – R_g plane. The blue line at $Z_{\text{max}} = 0.25 \text{ kpc}$ and red line at $Z_{\text{max}} = 2 \text{ kpc}$ mark our geometric cuts for the thin and thick disk selections, respectively.

trend than applying either cut alone. We combine both criteria to select “pure” thin and thick disk populations as follows:

- Thin disk: $[\alpha/\text{Fe}]$ below the black line in Figure 1(c) and $Z_{\text{max}} < 0.25 \text{ kpc}$
- Thick disk: $[\alpha/\text{Fe}]$ above the black line in Figure 1(c) and $Z_{\text{max}} > 2 \text{ kpc}$.

This yields 18,363 thin disk stars and 24,210 thick disk stars (7.4% and 9.8% of the total clean sample, respectively). Their distributions in the $[\alpha/\text{Fe}]$ – $[\text{Fe}/\text{H}]$ and Z_{max} – R_g planes are shown in Section 3.

Figure 2 presents the $[\text{Fe}/\text{H}]$ – R_g and age distributions of the selected subsamples. The thin disk shows a clear negative metallicity gradient centered around solar metallicity. In contrast, the thick disk is more metal-poor (typical $[\text{Fe}/\text{H}] \sim -0.6 \text{ dex}$) and exhibits a slightly positive gradient. Thick disk stars are also more centrally concentrated and older, consistent with the inside-out formation scenario.

2.3. Calculation of the MGAR

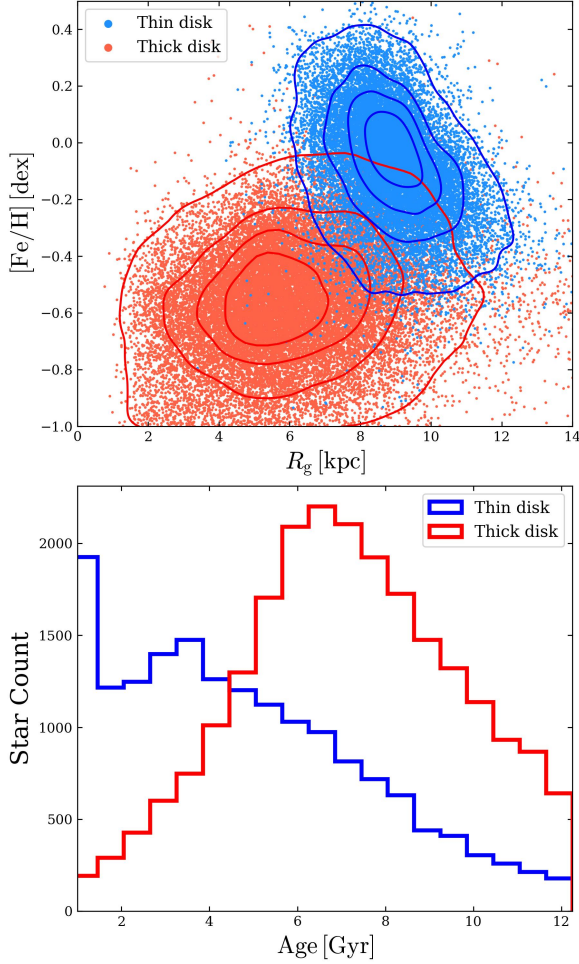


Figure 2. $[\text{Fe}/\text{H}]$ – R_g and age distributions for the selected thin (blue) and thick (red) disk stars. **Upper panel:** $[\text{Fe}/\text{H}]$ vs. guiding center radius R_g . Thin disk stars with near-solar metallicity show a gradient decreasing outward, while thick disk stars are more metal-poor (typical $[\text{Fe}/\text{H}] \sim -0.6$ dex) and exhibit a mildly positive gradient; **Lower panel:** Age distribution. Thin disk stars are generally younger than thick disk stars. The presence of old, metal-poor stars concentrated in the inner disk, and young, solar-metallicity stars in the outer disk, is consistent with inside-out disk formation.

We calculate the metallicity gradient $d[\text{Fe}/\text{H}]/dR_g$ across nine equal-width age bins from 1 to 12.25 Gyr. Following V21, we apply the weighted ordinary least squares (OLS) regression from SciPy (Virtanen et al. 2020) using weights $w_i = 1/\Delta[\text{Fe}/\text{H}]_i^2$, where $\Delta[\text{Fe}/\text{H}]$ is the absolute metallicity uncertainty. The uncertainty in the fitted gradient is derived from the covariance matrix.

To evaluate the effect of uncertainties in $[\text{Fe}/\text{H}]$, R_g , and age simultaneously, we perform an independent Bayesian fit in Appendix A using the PyMC package (PyMC-Devs 2025). This test incorporates all three sources of uncertainty and confirms that the MGAR trends in both disks are robust.

3. RESULTS

Figure 3 presents the MGAR in the thin and thick disks, compared to the results of V21 (black points). Gradient fits for each mono-age population are shown in detail in Figure 4. Larger uncertainties—particularly for the oldest thin disk stars and the youngest thick disk populations—are primarily due to limited sample sizes (see the age histograms in Figure 2).

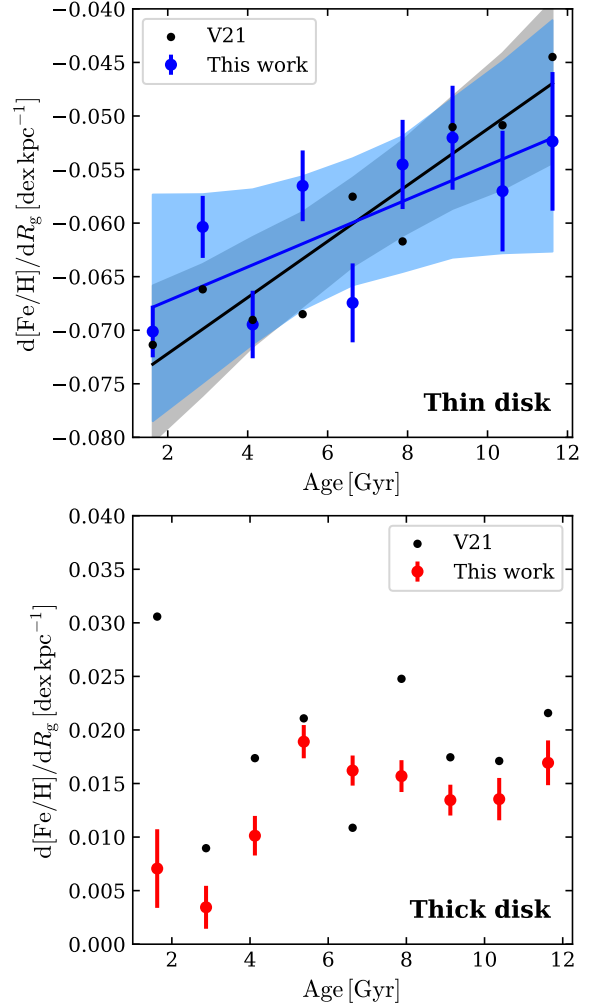


Figure 3. Metallicity gradient–age relation (MGAR) in the thin (top) and thick (bottom) disks, compared to the results of V21 (black dots). Error bars are derived from the covariance matrix of the weighted OLS fits. **Upper panel:** MGAR in the thin disk. The blue line shows our fitted trend, with a flattening rate of $0.0016 \text{ dex kpc}^{-1} \text{ Gyr}^{-1}$; the shaded region denotes the 98% highest density interval (HDI). The black line and gray shade show the fit for V21. Check the caption of Figure A1 in the Appendix for prior specifications. **Lower panel:** MGAR in the thick disk. Our results yield a mean positive gradient of $\sim 0.013 \text{ dex kpc}^{-1}$.

We also examine how the MGAR responds to variations in selection criteria and orbital integration configurations in Appendices B and C. Similar to V21, Appendix B shows that the flattening MGAR in the thin disk primarily originates from low- Z_{max} stars, which may be due to the favored migration for stars on the vertically coldest orbits (Solway et al. 2012; Vera-Ciro et al. 2014). Appendix C further demonstrates that the choice of Galactic potential Φ and solar circular velocity v_0 can affect the numerical values of MGAR in the thin disk, but the overall flattening trend remains robust.

3.1. Metallicity Gradient in the Thin Disk

The metallicity gradient in the thin disk gradually flattens as stellar age increases and aligns broadly with V21. The gradient of the youngest stars reaches $-0.07 \text{ dex kpc}^{-1}$ in agreement with V21 and other studies (Chen & Zhao 2020; Zhang et al. 2021; Wang et al. 2023b; Ratcliffe et al. 2023).

A comprehensive comparison of thin disk MGAR measurements using various stellar tracers is given in Wang et al. (2023b). Their Figure 5 highlights a distinctively V-shaped MGAR trend with a dip around $5 \sim 7 \text{ Gyr}$ in studies based on main-sequence turn-off (MSTO) stars (e.g., Xiang et al. 2015; Wang et al. 2019), which is absent in our result using RGB and RC stars. V-shapes with a dip around 2 Gyr have been reported using red giant stars from CoRoGEE (Anders et al. 2017) and APOGEE (Anders et al. 2023). The existence and characteristics of this V-shape remain unclear and warrant further investigation with larger samples.

3.2. Metallicity Gradient in the Thick Disk

The gradients in the thick disk are generally positive across all ages, with a mean value of $\sim 0.013 \text{ dex kpc}^{-1}$. Interestingly, the gradient increases steadily with decreasing stellar age, reaching a peak of $\sim 0.019 \text{ dex kpc}^{-1}$ at $\sim 5.4 \text{ Gyr}$, but flattens at younger ages. This flattening is likely driven by a population of young, metal-poor thick disk stars. As shown in the fourth row of Figure 4, these stars—located at $R_g > 10 \text{ kpc}$ —contribute to suppressed gradients in the young thick disk panels. Our test confirms that thick disk stars at $R_g > 10 \text{ kpc}$ exhibit a negative gradient ($\sim -0.02 \text{ dex kpc}^{-1}$). Removing these stars reduces the flattening at young ages and raises the gradient values to $\sim 0.02 \text{ dex kpc}^{-1}$, but the overall MGAR trend remains. Overall, our results are consistent with V21, reaffirming the existence of a slightly positive MGAR in the thick disk.

4. DISCUSSION

4.1. Origin of the Flattening Gradient in the Thin Disk

As discussed in Section 1, radial migration—particularly churning—is a likely mechanism for redistributing stars after their formation, thereby contributing to the observed flattening of the MGAR (see Figure 3, upper panel). However, it remains uncertain whether the flattening primarily reflects stellar migration or intrinsic evolution in the ISM gradient over time.

Several studies have explored this question. Within the inside-out formation framework, Minchev et al. (2018) reconstructed stellar birth radii and found a gradual flattening of the birth metallicity gradient over time. Similar flattening trends have been observed in external galaxies, where more massive systems tend to show shallower gradients. The analytic model of Sharda et al. (2021a) captures this mass dependence, predicting that gradients measured in dex kpc^{-1} flatten with increasing stellar mass, while gradients in $\text{dex } r_e^{-1}$ follow a U-shape (r_e is the effective radius). Interestingly, applying this model to MW-like galaxies yields opposite gradient evolutions depending on assumptions: a *steepening* ISM gradient over time, or a *flattening* gradient if the gas velocity dispersion is scaled by $(1+z)^{-1}$, to account for possible overestimates in star formation rates (Sharda et al. 2021b). These discrepancies highlight the need for more robust theoretical treatments.

Recent FIRE2 simulations challenged the migration-driven scenario. Graf et al. (2025) found that the present-day MGAR closely follows the evolution of the stellar birth gradient (or ISM gradient then), suggesting minimal impact from radial migration. As shown in the simulations of Graf et al. (2024), gas-phase metals are efficiently mixed by turbulence and diffusion before star formation, suppressing spatial metallicity differences. As a result, prominent metallicity gradients appear only after the disk settles and turbulence decreases. This interpretation emphasizes gas-phase processes over stellar redistribution.

Figure 5 contrasts our observed MGAR with several of the previously mentioned studies (solid lines for MGARs, dashed lines for stellar birth/ISM gradient evolutions). In the upper panel, we compare our thin disk MGAR with the reconstructed birth gradients from Ratcliffe et al. (2023) and Lu et al. (2024). The MGAR steepens and the birth gradients flatten as stellar age decreases, and they converge near $-0.07 \text{ dex kpc}^{-1}$ for the youngest stars, where migration is negligible. Lu et al. (2024) proposed that the sharp steepening of birth gradient between 12 and 10 Gyr in Ratcliffe et al. (2023) could be attributed to the Gaia–Enceladus/Sausage merger (Helmi et al. 2018; Belokurov et al. 2018).

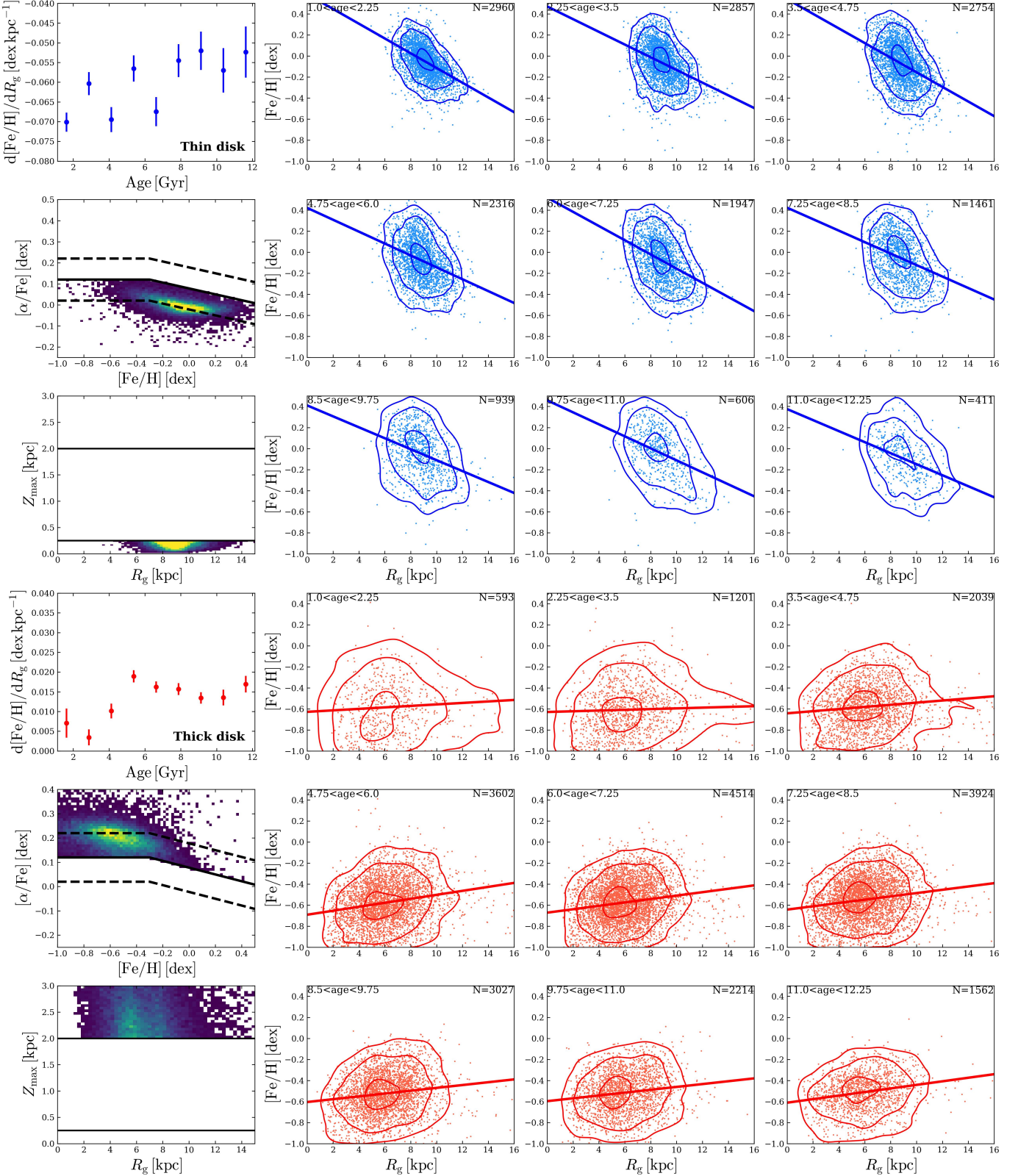


Figure 4. Metallicity gradient fits for mono-age populations in the thin (top three rows) and thick (bottom three rows) disks. Each panel in the right three columns shows the $[\text{Fe}/\text{H}]$ – R_g distribution for a specific age bin, with 20%, 80%, and 95% contours and the size of the mono-age population. The first column displays the MGARs, $[\alpha/\text{Fe}]$ – $[\text{Fe}/\text{H}]$, and Z_{max} – R_g distributions for the two disk populations. Notably, spurred contours appear in the fourth row at $R_g > 10$ kpc, which tend to suppress the positive gradient. After removing these stars, the thick disk gradient increases from ~ 0.013 dex kpc $^{-1}$ to ~ 0.02 dex kpc $^{-1}$ with reduced age-dependent fluctuation.

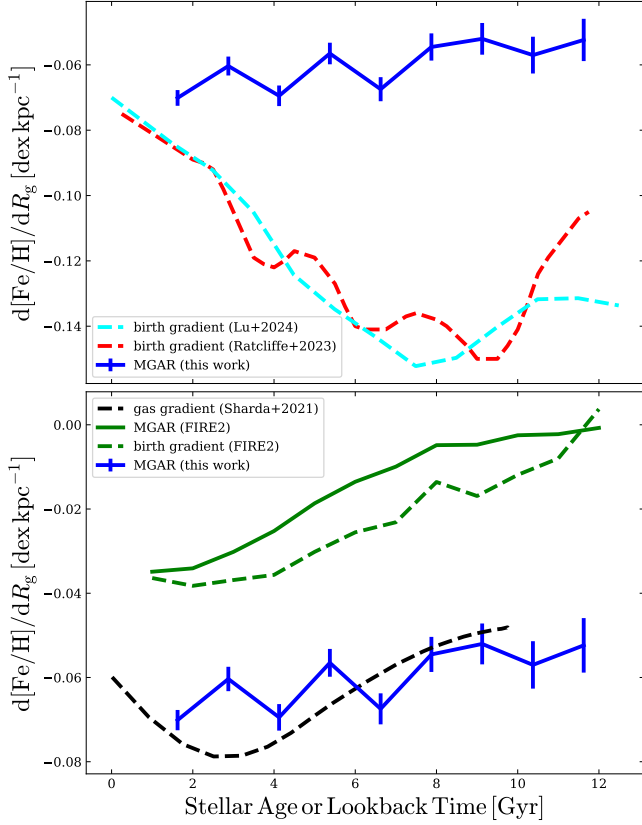


Figure 5. Comparison between our observed MGAR in the thin disk and literature results (solid lines for MGARs, dashed lines for stellar birth/ISM gradient evolutions). **Upper panel:** MGAR in the thin disk compared with reconstructed birth gradients from Ratcliffe et al. (2023) and Lu et al. (2024). The divergence between the MGAR and birth gradient at old ages may reflect the cumulative effect of churning. The gradient of the youngest stars aligns with the birth gradients ($\sim -0.07 \text{ dex kpc}^{-1}$) since little migration could occur. **Lower panel:** MGAR compared with two results predicting steepening gradients: the gas-phase evolution from Sharda et al. (2021b) and the birth gradient from FIRE2 simulations (Graf et al. 2024), we also plot the MGAR from the FIRE2 simulations. See the text for further discussion.

In the lower panel of Figure 5, we compare our MGAR in the thin disk to the gas-phase gradient evolution predicted by Sharda et al. (2021b) and to both the birth gradient and MGAR from FIRE2 simulations (Graf et al. 2024). Our observed MGAR agrees broadly with Sharda et al. (2021b) except for the upturn at younger ages ($\lesssim 3 \text{ Gyr}$), which is likely due to enhanced dilution from late gas accretion. Within FIRE2, the similarity between the MGAR (green solid line) and the birth gradient (green dashed line) suggests minimal churning. Similar to other studies, our MGAR appears significantly steeper than that of FIRE2, possibly due to uncertainties in Galactic distance measurements or an ear-

lier disk settling in the MW compared to FIRE2 galaxies or nearby MW analogs (Graf et al. 2024).

4.2. Origin of the Positive Gradient in the Thick Disk

The thick disk likely formed in the early evolutionary stages of the MW, when the disk was gas-rich and dynamically turbulent. Under such conditions, it is plausible that a weakly positive radial metallicity gradient could emerge. Simulations from the FIRE2 suite suggest that strong stellar feedback, especially from early starbursts, can drive metal-enriched outflows into the outer disk, leading to such positive gradients (Sun et al. 2024). The accretion of pristine gas into the MW center during early epochs may also contribute to forming a positive metallicity gradient (Cresci et al. 2010; Curir et al. 2012). Recent JWST observations show positive metallicity gradient ($0.165 \text{ dex kpc}^{-1}$) at $z \sim 3$ (Wang et al. 2022b). For even higher redshifts, Venturi et al. (2024) measured slightly positive gradients ($-0.03 \sim 0.14 \text{ dex kpc}^{-1}$) in $6 < z < 8$, while Li et al. (2025) reported flattening negative gradients ($-0.53 \text{ dex kpc}^{-1}$ to $-0.34 \text{ dex kpc}^{-1}$) from $z \approx 7$ to $z \approx 6$ (their Figure 2) and suggest that the slightly positive gradients in Venturi et al. (2024) are resulted from merging systems.

Given the relatively small positive gradient we observe ($\sim 0.013 \text{ dex kpc}^{-1}$), another possibility is that the thick disk initially had no radial gradient. This would align with the clumpy formation scenario of the thick disk, where giant clumps heat the galactic disk and violent perturbations erase chemodynamical relations during the formation of the thick disk (e.g., Inoue & Saitoh 2014).

The flattening gradient with increasing age for thick disk stars older than $\sim 5.4 \text{ Gyr}$ might reflect the cumulative effects of radial migration within the thick disk (Solway et al. 2012; Halle et al. 2018). Early turbulence and mixing could have dispersed stars from their birth radii, weakening any original gradient and leading to the flatter distributions seen today.

Future studies could apply parameterized models such as the one used in Frankel et al. (2020) to improve the robustness of MGAR measurements. Such parameterized models and the multi-ring chemical evolution model in Johnson et al. (2021) may also help distinguish between different birth gradient evolution scenarios shown in Figure 5.

5. CONCLUSIONS

Following the methodology of Vickers et al. (2021, hereafter V21), we select chemically and kinematically “pure” thin and thick disk stars from LAMOST DR8 and compute the radial metallicity gradient

($d[\text{Fe}/\text{H}]/dR_g$) across mono-age populations to investigate the metallicity gradient–age relation (MGAR) in both disks.

For the thin disk, we confirm a monotonic flattening of the MGAR with increasing stellar age. The fitted flattening rate is $\sim 0.0016 \text{ dex kpc}^{-1} \text{ Gyr}^{-1}$, which is lower than the value reported by V21 ($0.003 \text{ dex kpc}^{-1} \text{ Gyr}^{-1}$). The youngest thin disk stars exhibit a gradient of $-0.07 \text{ dex kpc}^{-1}$, consistent with V21 and other studies. In contrast, the thick disk shows a generally positive MGAR with a mean value of $\sim 0.013 \text{ dex kpc}^{-1}$, also in agreement with V21. Notably, we observe a flattening of the gradient for young thick disk stars (1.0–4.75 Gyr), likely due to a population of young, metal-poor stars at large guiding radii.

These MGAR trends reflect distinct chemodynamical histories for the MW’s thin and thick disks. In particular, the thin disk MGAR offers a valuable diagnostic for distinguishing between different formation scenarios, such as the “inside-out” model with significant radial migration and the “upside-down” model with minimal migration. Future studies using larger stellar samples with more precise ages, alongside improved chemodynamical modeling, will be crucial for disentangling these

processes and refining our understanding of the Galaxy’s formation history.

6. ACKNOWLEDGEMENTS

We thank the developers and maintainers of the following software libraries, which were used in this work: *ArviZ* (Kumar et al. 2019), *Astropy* (Astropy Collaboration et al. 2022), *galpy* (Bovy 2015), *matplotlib* (Hunter 2007), *NumPy* (Harris et al. 2020), *pandas* (pandas development team 2020; Wes McKinney 2010), *PyMC* (PyMC-Devs 2025), *seaborn* (Waskom 2021), and *scipy* (Virtanen et al. 2020).

The research presented here is partially supported by the National Natural Science Foundation of China under grant Nos. 12025302, 11773052, 11761131016; by China Manned Space Program with grant no. CMS-CSST-2025-A11; and by the “111” Project of the Ministry of Education of China under grant No. B20019. This work has made use of the Gravity Supercomputer at the Department of Astronomy, Shanghai Jiao Tong University.

7. DATA AVAILABILITY

The LAMOST DR8 astrometric and spectroscopic data, as well as the RGB and RC age catalog, are publicly available at: <http://www.lamost.org/dr8/v1.0/doc/vac>.

REFERENCES

- Anders, F., Chiappini, C., Minchev, I., et al. 2017, *A&A*, 600, A70, doi: [10.1051/0004-6361/201629363](https://doi.org/10.1051/0004-6361/201629363)
- Anders, F., Gispert, P., Ratcliffe, B., et al. 2023, *A&A*, 678, A158, doi: [10.1051/0004-6361/202346666](https://doi.org/10.1051/0004-6361/202346666)
- Astropy Collaboration, Price-Whelan, A. M., Lim, P. L., et al. 2022, *ApJ*, 935, 167, doi: [10.3847/1538-4357/ac7c74](https://doi.org/10.3847/1538-4357/ac7c74)
- Belokurov, V., Erkal, D., Evans, N. W., Koposov, S. E., & Deason, A. J. 2018, *MNRAS*, 478, 611, doi: [10.1093/mnras/sty982](https://doi.org/10.1093/mnras/sty982)
- Binney, J., & Tremaine, S. 2008, *Galactic Dynamics: Second Edition*
- Bovy, J. 2015, *ApJS*, 216, 29, doi: [10.1088/0067-0049/216/2/29](https://doi.org/10.1088/0067-0049/216/2/29)
- Chen, Y. Q., & Zhao, G. 2020, *MNRAS*, 495, 2673, doi: [10.1093/mnras/staa1079](https://doi.org/10.1093/mnras/staa1079)
- Cresci, G., Mannucci, F., Maiolino, R., et al. 2010, *Nature*, 467, 811, doi: [10.1038/nature09451](https://doi.org/10.1038/nature09451)
- Curir, A., Lattanzi, M. G., Spagna, A., et al. 2012, *A&A*, 545, A133, doi: [10.1051/0004-6361/201118558](https://doi.org/10.1051/0004-6361/201118558)
- Frankel, N., Sanders, J., Ting, Y.-S., & Rix, H.-W. 2020, *ApJ*, 896, 15, doi: [10.3847/1538-4357/ab910c](https://doi.org/10.3847/1538-4357/ab910c)
- Gilmore, G., & Reid, N. 1983, *MNRAS*, 202, 1025, doi: [10.1093/mnras/202.4.1025](https://doi.org/10.1093/mnras/202.4.1025)
- Graf, R. L., Wetzel, A., Bailin, J., & Orr, M. E. 2024, *arXiv e-prints*, arXiv:2410.21377, doi: [10.48550/arXiv.2410.21377](https://doi.org/10.48550/arXiv.2410.21377)
- Graf, R. L., Wetzel, A., Bellardini, M. A., & Bailin, J. 2025, *ApJ*, 981, 47, doi: [10.3847/1538-4357/adacd7](https://doi.org/10.3847/1538-4357/adacd7)
- Halle, A., Di Matteo, P., Haywood, M., & Combes, F. 2018, *A&A*, 616, A86, doi: [10.1051/0004-6361/201832603](https://doi.org/10.1051/0004-6361/201832603)
- Harris, C. R., Millman, K. J., van der Walt, S. J., et al. 2020, *Nature*, 585, 357, doi: [10.1038/s41586-020-2649-2](https://doi.org/10.1038/s41586-020-2649-2)
- Hayden, M. R., Bovy, J., Holtzman, J. A., et al. 2015, *ApJ*, 808, 132, doi: [10.1088/0004-637X/808/2/132](https://doi.org/10.1088/0004-637X/808/2/132)
- Helmi, A., Babusiaux, C., Koppelman, H. H., et al. 2018, *Nature*, 563, 85, doi: [10.1038/s41586-018-0625-x](https://doi.org/10.1038/s41586-018-0625-x)
- Hunter, J. D. 2007, *Computing in Science & Engineering*, 9, 90, doi: [10.1109/MCSE.2007.55](https://doi.org/10.1109/MCSE.2007.55)
- Inoue, S., & Saitoh, T. R. 2014, *MNRAS*, 441, 243, doi: [10.1093/mnras/stu544](https://doi.org/10.1093/mnras/stu544)
- Johnson, J. W., Weinberg, D. H., Vincenzo, F., et al. 2021, *MNRAS*, 508, 4484, doi: [10.1093/mnras/stab2718](https://doi.org/10.1093/mnras/stab2718)

- Kumar, R., Carroll, C., Hartikainen, A., & Martin, O. 2019, *Journal of Open Source Software*, 4, 1143, doi: [10.21105/joss.01143](https://doi.org/10.21105/joss.01143)
- Li, Z., Cai, Z., Wang, X., et al. 2025, arXiv e-prints, arXiv:2506.12129, doi: [10.48550/arXiv.2506.12129](https://doi.org/10.48550/arXiv.2506.12129)
- Lu, Y. L., Minchev, I., Buck, T., et al. 2024, *MNRAS*, 535, 392, doi: [10.1093/mnras/stae2364](https://doi.org/10.1093/mnras/stae2364)
- Matteucci, F. 2021, *A&A Rv*, 29, 5, doi: [10.1007/s00159-021-00133-8](https://doi.org/10.1007/s00159-021-00133-8)
- Matteucci, F., & Francois, P. 1989, *MNRAS*, 239, 885, doi: [10.1093/mnras/239.3.885](https://doi.org/10.1093/mnras/239.3.885)
- Mayor, M. 1976, *A&A*, 48, 301
- Minchev, I., Anders, F., Recio-Blanco, A., et al. 2018, *MNRAS*, 481, 1645, doi: [10.1093/mnras/sty2033](https://doi.org/10.1093/mnras/sty2033)
- Nomoto, K., Kobayashi, C., & Tominaga, N. 2013, *ARA&A*, 51, 457, doi: [10.1146/annurev-astro-082812-140956](https://doi.org/10.1146/annurev-astro-082812-140956)
- pandas development team, T. 2020, pandas-dev/pandas: Pandas, latest, Zenodo, doi: [10.5281/zenodo.3509134](https://doi.org/10.5281/zenodo.3509134)
- PyMC-Devs. 2025, PyMC, Zenodo, doi: [10.5281/zenodo.14611282](https://doi.org/10.5281/zenodo.14611282)
- Ratcliffe, B., Minchev, I., Anders, F., et al. 2023, *MNRAS*, 525, 2208, doi: [10.1093/mnras/stad1573](https://doi.org/10.1093/mnras/stad1573)
- Schönrich, R., & Aumer, M. 2017, *MNRAS*, 472, 3979, doi: [10.1093/mnras/stx2189](https://doi.org/10.1093/mnras/stx2189)
- Sellwood, J. A., & Binney, J. J. 2002, *MNRAS*, 336, 785, doi: [10.1046/j.1365-8711.2002.05806.x](https://doi.org/10.1046/j.1365-8711.2002.05806.x)
- Sharda, P., Krumholz, M. R., Wisnioski, E., et al. 2021a, *MNRAS*, 504, 53, doi: [10.1093/mnras/stab868](https://doi.org/10.1093/mnras/stab868)
- . 2021b, *MNRAS*, 502, 5935, doi: [10.1093/mnras/stab252](https://doi.org/10.1093/mnras/stab252)
- Solway, M., Sellwood, J. A., & Schönrich, R. 2012, *MNRAS*, 422, 1363, doi: [10.1111/j.1365-2966.2012.20712.x](https://doi.org/10.1111/j.1365-2966.2012.20712.x)
- Sun, X., Wang, X., Ma, X., et al. 2024, arXiv e-prints, arXiv:2409.09290, doi: [10.48550/arXiv.2409.09290](https://doi.org/10.48550/arXiv.2409.09290)
- Venturi, G., Carniani, S., Parlanti, E., et al. 2024, *A&A*, 691, A19, doi: [10.1051/0004-6361/202449855](https://doi.org/10.1051/0004-6361/202449855)
- Vera-Ciro, C., D’Onghia, E., Navarro, J., & Abadi, M. 2014, *ApJ*, 794, 173, doi: [10.1088/0004-637X/794/2/173](https://doi.org/10.1088/0004-637X/794/2/173)
- Vickers, J. J., Shen, J., & Li, Z.-Y. 2021, *ApJ*, 922, 189, doi: [10.3847/1538-4357/ac27a9](https://doi.org/10.3847/1538-4357/ac27a9)
- Virtanen, P., Gommers, R., Oliphant, T. E., et al. 2020, *Nature Methods*, 17, 261, doi: [10.1038/s41592-019-0686-2](https://doi.org/10.1038/s41592-019-0686-2)
- Wang, C., Huang, Y., Yuan, H., et al. 2022a, *ApJS*, 259, 51, doi: [10.3847/1538-4365/ac4df7](https://doi.org/10.3847/1538-4365/ac4df7)
- Wang, C., Huang, Y., Zhou, Y., & Zhang, H. 2023a, *A&A*, 675, A26, doi: [10.1051/0004-6361/202245809](https://doi.org/10.1051/0004-6361/202245809)
- Wang, C., Yuan, H., Xiang, M., et al. 2023b, *A&A*, 674, A129, doi: [10.1051/0004-6361/202245761](https://doi.org/10.1051/0004-6361/202245761)
- Wang, C., Liu, X. W., Xiang, M. S., et al. 2019, *MNRAS*, 482, 2189, doi: [10.1093/mnras/sty2797](https://doi.org/10.1093/mnras/sty2797)
- Wang, X., Jones, T., Vulcani, B., et al. 2022b, *ApJL*, 938, L16, doi: [10.3847/2041-8213/ac959e](https://doi.org/10.3847/2041-8213/ac959e)
- Waskom, M. L. 2021, *Journal of Open Source Software*, 6, 3021, doi: [10.21105/joss.03021](https://doi.org/10.21105/joss.03021)
- Wes McKinney. 2010, in *Proceedings of the 9th Python in Science Conference*, ed. Stéfan van der Walt & Jarrod Millman, 56 – 61, doi: [10.25080/Majora-92bf1922-00a](https://doi.org/10.25080/Majora-92bf1922-00a)
- Xiang, M.-S., Liu, X.-W., Yuan, H.-B., et al. 2015, *Research in Astronomy and Astrophysics*, 15, 1209, doi: [10.1088/1674-4527/15/8/009](https://doi.org/10.1088/1674-4527/15/8/009)
- Yu, J., Sellwood, J. A., Pryor, C., Chen, L., & Hou, J. 2012, *ApJ*, 754, 124, doi: [10.1088/0004-637X/754/2/124](https://doi.org/10.1088/0004-637X/754/2/124)
- Zhang, H., Chen, Y., & Zhao, G. 2021, *ApJ*, 919, 52, doi: [10.3847/1538-4357/ac0e92](https://doi.org/10.3847/1538-4357/ac0e92)

APPENDIX

Here, we present how our results vary with different fitting methods, thin/thick selections, and galactic setups.

A. FITTING MGAR INCORPORATING ALL UNCERTAINTIES

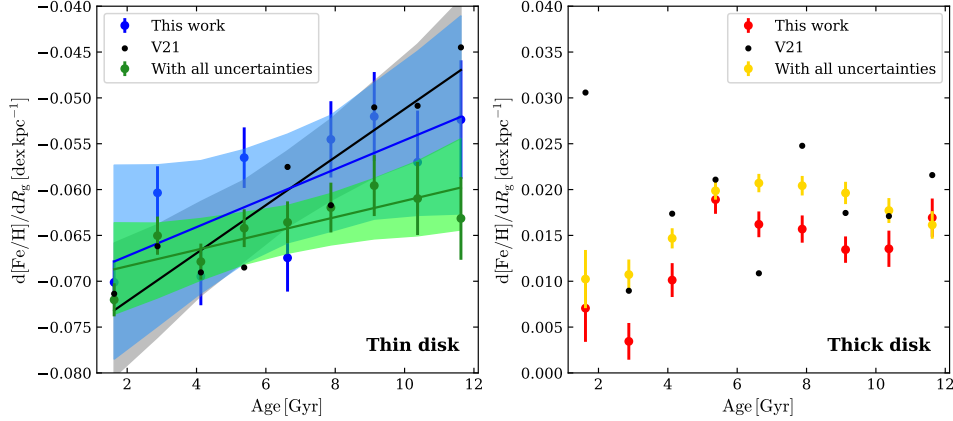


Figure A1. MGAR results from a Bayesian model that incorporates uncertainties in $[\text{Fe}/\text{H}]$, guiding radius R_g , and stellar age τ . **Left panel:** MGARs in the thin disk. Blue points show the fiducial OLS results (this work), black points show V21, and forest green points are from the Bayesian model. Shaded regions denote the 98% highest density intervals (HDI) for each fitted line. All fits adopt the same prior: slope $\sim \mathcal{N}(0, 2^2)$, intercept $\sim \mathcal{N}(0, 2^2)$. Solid line fitting model: gradient $\sim \mathcal{N}(\text{intercept} + \text{slope} \times \text{age bin center}, \epsilon^2)$, where $\epsilon \sim \text{HalfCauchy}(\beta = 5)$. **Right panel:** MGARs in the thick disk: OLS fitting (red), V21 (black), and the Bayesian model (gold).

We assess how uncertainties in $[\text{Fe}/\text{H}]$, guiding radius R_g , and stellar age τ affect the derived MGAR by implementing a Bayesian fitting procedure using PyMC (PyMC-Devs 2025). The absolute $[\text{Fe}/\text{H}]$ uncertainty ($\Delta[\text{Fe}/\text{H}]$) is taken directly from the LAMOST DR8 catalog. The absolute uncertainty in R_g (ΔR_g) is estimated by propagating position and velocity errors through 100 Monte Carlo realizations. The absolute stellar age uncertainty ($\Delta\tau$) is from Wang et al. (2023a), which includes an intrinsic method error of $\sim 20\%$ (i.e., $\delta\tau \gtrsim 20\%$).

We model the relation $[\text{Fe}/\text{H}] \sim \nabla R_g + b$, where ∇ is the metallicity gradient and b is the intercept, assuming a truncated normal likelihood $\tilde{\mathcal{N}}$:

$$[\text{Fe}/\text{H}]_{\text{obs}} \sim \tilde{\mathcal{N}}([\text{Fe}/\text{H}] \mid \nabla R_g + b, \Sigma^2), \quad (\text{A1})$$

with the observed $[\text{Fe}/\text{H}]_{\text{obs}}$ truncated to the range $[-1.0, 0.5]$ dex.

- Uncertainty in R_g : We treat R_g as a latent variable drawn from a truncated normal distribution:

$$R_g \sim \tilde{\mathcal{N}}(R_g \mid R_{g,\text{obs}}, \Delta R_g^2), \quad R_g \in [0, 20] \text{ kpc}. \quad (\text{A2})$$

- Uncertainty in $[\text{Fe}/\text{H}]$: The total variance Σ combines intrinsic scatter σ and absolute $[\text{Fe}/\text{H}]$ uncertainty:

$$\Sigma^2 \propto \sigma^2 + \Delta[\text{Fe}/\text{H}]^2. \quad (\text{A3})$$

- Uncertainty in age: To account for $\Delta\tau$, we apply a weight based on the probability that the true age lies within the assigned age bin. Assuming a truncated normal distribution for the true age within $[0, 13]$ Gyr, the effective variance Σ in Equation A1 becomes:

$$\Sigma^2 = \frac{\sigma^2 + \Delta[\text{Fe}/\text{H}]^2}{\left[\int_{\text{bin}} \tilde{\mathcal{N}}(\tau \mid \tau_{\text{obs}}, \Delta\tau^2) d\tau \right]^2}. \quad (\text{A4})$$

- Priors: The model uses the following priors:

$$\nabla \sim \mathcal{N}(0, 0.5^2), \quad b \sim \mathcal{N}(0, 0.5^2), \quad \sigma \sim \text{HalfNormal}(0, 0.4^2).$$

Posterior sampling is performed using the PyMC package. The uncertainty of the gradient ∇ is the standard deviation of the posterior.

Figure A1 compares the MGAR obtained from this Bayesian model to our fiducial (OLS) results and V21 results. We find that our Bayesian model reduces fluctuations in the MGAR for both the thin and thick disks. For the thin disk, the Bayesian MGAR trend shows the lowest flattening rate. In the thick disk, the Bayesian MGAR shifts upward, though the age-dependent pattern remains similar. These results confirm that the qualitative MGAR trends are robust when all key uncertainties are included.

B. TESTS OF CHEMICAL/ Z_{MAX} CUT

We examine how changes to the chemical ($[\alpha/\text{Fe}]$ – $[\text{Fe}/\text{H}]$) and geometric (i.e., Z_{max}) selection criteria affect the MGAR.

In Figure B1, we adjust the chemical division line in the $[\alpha/\text{Fe}]$ – $[\text{Fe}/\text{H}]$ plane by ± 0.1 dex without applying the Z_{max} cut. The top row shows the resulting MGARs under these altered chemical selections.

Figure B2 explores the effect of purely geometric selections, dividing the sample into four Z_{max} bins: (0–0.25), (0.25–0.8), (0.8–2), and (2–6) kpc, with no chemical cut applied. The first and second columns of Figure B2 show that the observed MGAR flattening in the thin disk mainly comes from stars with low Z_{max} , which may be due to the preferred migration for stars on the vertically coldest orbits (Solway et al. 2012; Vera-Ciro et al. 2014).

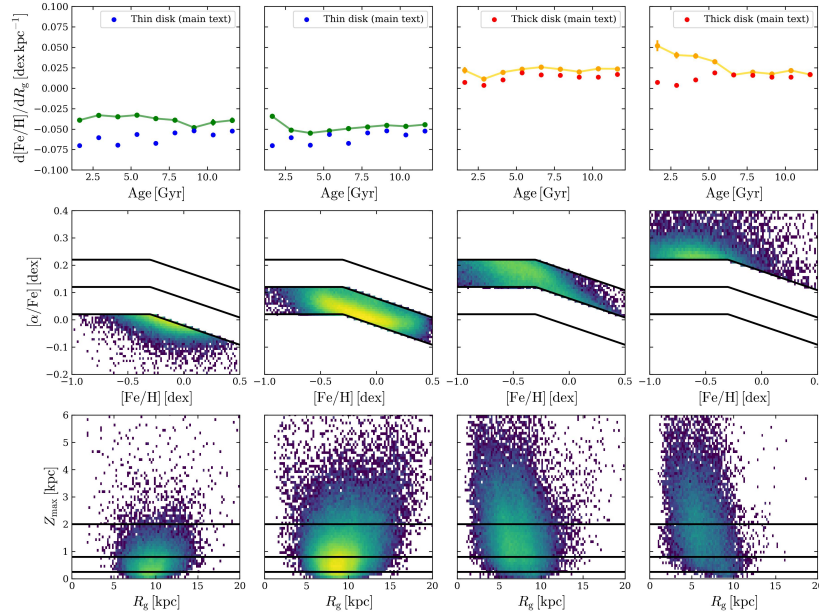


Figure B1. Effect of shifting the chemical division in the $[\alpha/\text{Fe}]$ – $[\text{Fe}/\text{H}]$ plane by ± 0.1 dex, blue and red dots are MGAR results from the main text. The top row displays the MGAR results without Z_{max} cut. The second row shows the chemical-only selection.

C. SENSITIVITY TO GALACTIC POTENTIAL AND SOLAR PARAMETERS

The canonical results in the main text use $\Phi = \text{MWPotential2014}$ as the Galactic potential, a solar Galactocentric radius of $R_0 = 8.27$ kpc, and a circular velocity of $v_0 = 236 \text{ km s}^{-1}$ when calculating R_g . To test the robustness of our results, we vary each of these parameters while keeping the others fixed, as shown in Figure C1.

In the first row, we adopt three different Galactic potentials available in *galpy*: *MWPotential2014*, *McMillan17*, and *Irrgang13I*. In the second row, we vary the solar radius R_0 across 8.27, 7.0, and 9.5 kpc. In the third row, we test $v_0 = 236, 260$, and 200 km s^{-1} . The resulting MGARs remain largely consistent across these configurations. We

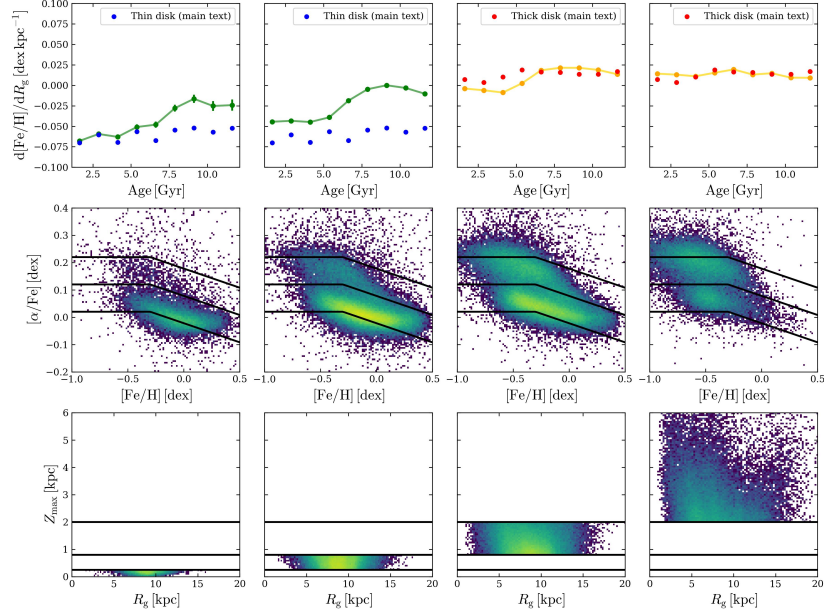


Figure B2. MGAR results for subsamples selected solely by Z_{\max} , with no chemical cut applied. The four columns correspond to $Z_{\max} = (0-0.25), (0.25-0.8), (0.8-2),$ and $(2-6)$ kpc. The flattening MGAR trend in the thin disk is mainly contributed by stars with low Z_{\max} .

find that while the numerical values of the MGAR in the thin disk are sensitive to the adopted Φ and v_0 , the overall MGAR remains robust across all panels in Figure C1.

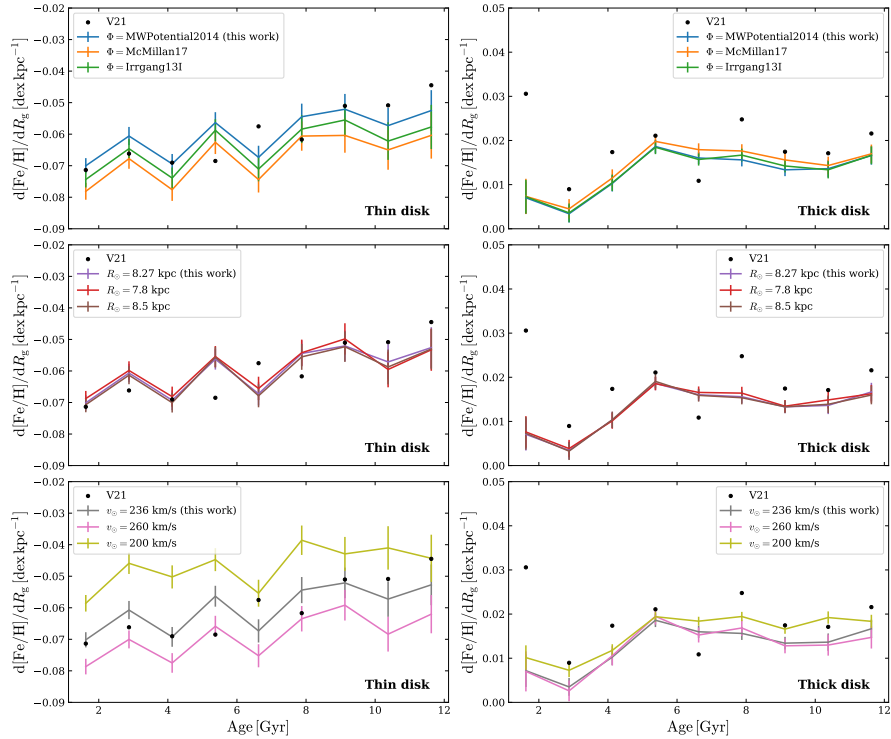


Figure C1. Robustness test of the MGAR under different Galactic configurations. The three rows correspond to variations in: (1) Galactic potential models used in *galpy* (MWPotential2014, McMillan17, Irrgang13I); (2) solar Galactocentric radius R_0 (8.27, 7.0, and 9.5 kpc); and (3) solar circular velocity v_0 (236, 260, and 200 km s^{-1}). The canonical setup in the main text adopts $\Phi = \text{MWPotential2014}$, $R_0 = 8.27$ kpc, and $v_0 = 236 \text{ km s}^{-1}$. The thin disk MGAR is most sensitive to Φ and v_0 .